A Comparison of Dynamic Flow Separation on Non-Slender Delta Wings During Axial Gusts

David E. Rival and Matthew Marzanek
Department of Mechanical and Materials Engineering
Queen's University, Kingston, Ontario
CANADA

d.e.rival@queensu.ca

ABSTRACT

In this paper we examine the effects of axial gusts on a generic UCAV configuration. The experiments are conducted at a Reynolds number of 300,000 using a large, optical towing-tank facility. Instantaneous force and moment measurements, pressure distributions and particle image velocimetry are used to extract critical features of the dynamic flow separation process for both gust events. For the axial-gust case, force augmentation both during and after the gust is shown to be dependent on the initial separation topology, with strong sensitivity at an angle of attack of 30°. It is shown that lift enhancement results from initially separated flow near the wing apex reattaching during the gust. Surface pressure measurements show that the reattachment is driven by a strong favorable pressure gradient that is maintained after the gust ends. The equations governing near-wall vortex dynamics state that vorticity flux from the wall increases with favorable pressure gradients, indirectly predicting an increase in circulation near the wing surface during a streamwise gust. However, circulation obtained through Particle Image Velocimetry (PIV) on the z/c = 0.1, 0.3, and 0.5 spanwise sections does not support this prediction, rather showing that the circulation in the wake (near the wing surface) remains nearly constant throughout the gust.

1. INTRODUCTION

Swept wings are prevalent on nearly all modern jet aircraft due to their improved efficiency at transonic speeds. In particular, non-slender sweep angles (<55°) and thick cross-sections are common traits in prototype blended bodies and unmanned combat aerial vehicles (UCAVs) (Liebeck, 2004; Cummings and Schuette, 2010). Despite the ubiquity of this geometry, little is understood about the aerodynamic response of swept wings to strong gust events. Classical theory of swept wings is often limited to slender configurations at steady-state and moderate angles of attack. Such slender geometry, designated by their sweep angle greater than 55°, are thoroughly characterized (Polhamus, 1966; Earnshaw and Lawford, 1966; Brown and Michael Jr, 1955; Lee and Ho, 1990; Gursul, 2005). However, slender wings differ significantly in flow structure from their non-slender counterparts. These differences include leading-edge vortex (LEV) structures forming closer to the wing surface for non-slender sweep angles (Ol and Gharib, 2003; Gursul et al., 2005). As a direct result, the formation of 'dual' primary vortex structures can be observed for non-slender geometry at low incidence angles (Taylor et al., 2003). Research on the SACCON (Stability And Control CONfiguration) model by Konrath et al. (2010) and Cummings and Schuette (2012) provide comprehensive references for unsteady behavior of non-slender geometry, but further geometric simplification is required to make conclusions on the general dynamic-stall phenomenon for non-slender wings. More recently, Le Provost et al. (2018) used a network of pressure sensors to predict roll moment on a USAS geometry (hybrid of a Lockheed Martin ICE-101 planform with SACCON cross-section), and He et al. (2018) used pneumatic blowing to develop an active control model on similar geometry. The present work seeks to further generalize, and therefore a 45° delta wing with a NACA0012 cross-

section is chosen to represent a baseline abstraction of non-slender swept wings. Experiments by Gad-el Hak and Blackwelder (1985) were performed on the proposed geometry, using dye visualization to identify the leading-edge vortical structures. They found that the leading-edge vortices were formed from series of smaller vortices, but were less coherent/identifiable at higher angles of attack. Moreover, Gad-el Hak and Ho (1985) also studied the effects of pitching on a NACA0012 non-slender delta wing. They discovered a bifurcation in separation behavior as the reduced frequency (k) of pitching was increased. Reduced frequencies greater than π resulted in the formation of a strong coherent shedding vortex that in-turn kept the separation contained to a thin layer above the wing surface.

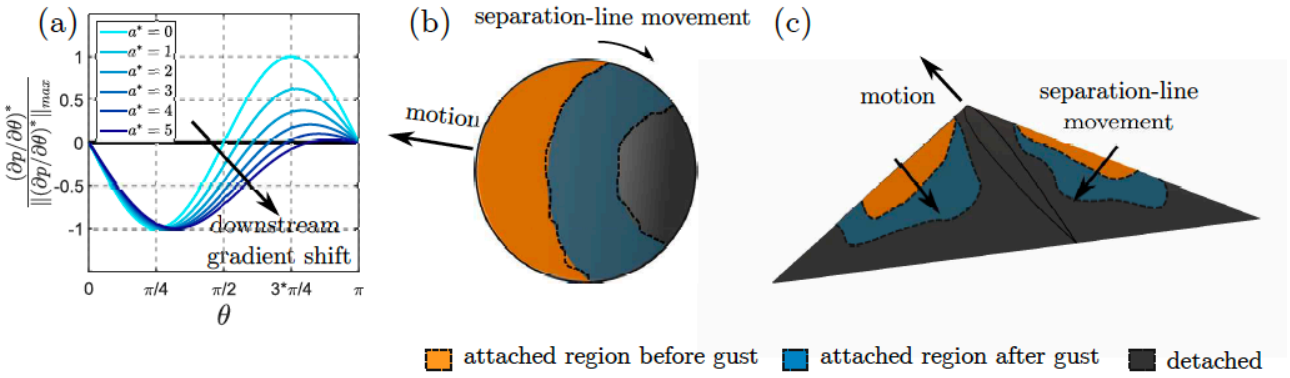

Figure 15-1: (a) Potential flow theory shows a reduction of adverse azimuthal pressure gradient on the sphere in (b) with increasing axial acceleration, a* , emulating a streamwise gust (adapted from Fernando et al. (2017)). (c) Outlines the hypothesized downstream separation-line movement due to the adverse pressure gradient reduction on a partially attached delta wing undergoing a streamwise gust.

The goal of this study is to understand the sensitivity of a NACA0012 non-slender geometry to axial acceleration, analogous to an aircraft subjected to a "head-on" or streamwise gust. Equivalence of varying inflow conditions to acceleration of the model is supported by results from Granlund et al. (2014), who compare an accelerating airfoil in a water tunnel, to a stationary airfoil in a wind tunnel with an accelerating freestream. When accounting for buoyancy forces in the wind tunnel, and inertial effects in the water tunnel, measured circulatory forces in each case were found to be in agreement, implying that a streamwise gust response can be studied through the acceleration of the test article. However, it should be noted that the study by Granlund et al. (2014) was strictly for a two-dimensional case, at a lower range of reduced frequency than tested in this study. The equivalence of transient inflow conditions to that of accelerating bodies remains poorly understood for complex three-dimensional flows. Nonetheless, the effect of acceleration is still relevant in understanding unsteady flow phenomenon in relation to non-slender delta wings, especially in application to highly maneuverable aerial vehicles with minimal wing loading. From the unsteady Euler equations, Fernando et al. (2017) demonstrated that spheres experience a favorable shift in azimuthal pressure gradient under acceleration, the premise of which is reproduced in Figure 1(a) and (b). Particle Image Velocimetry (PIV) in this study showed that the separation line moves downstream with increasing acceleration, supporting the potential-flow based prediction. Analogous to the sphere behavior, it is predicted here that regions of detached flow over the delta wing will shrink under acceleration, resulting in augmented values of normalized lift and pitching moment.

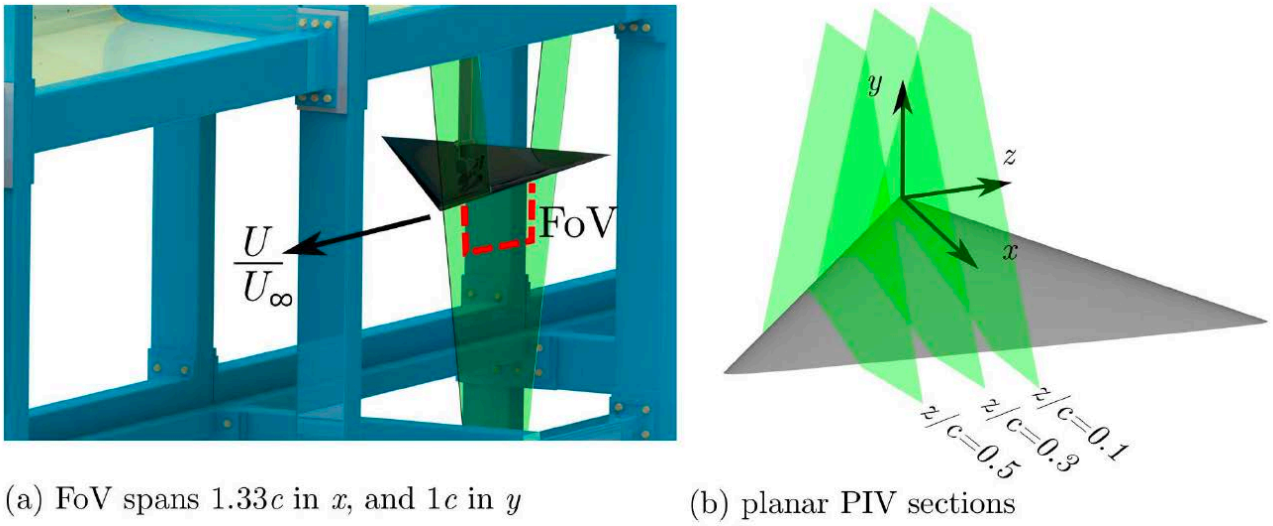

Figure 15-2: Experimental setup (a) of axial-gust experiments in the optical towing tank showing the Field of View (FoV), where (b) multiple time-resolved PIV cuts are performed over the wing span. Direct force/moment and pressure measurements are carried out concurrently.

2. EXPERIMENTAL METHODS

A combination of time-resolved force, pressure and PIV measurements are used to capture the dynamic-stall characteristics of the swept-wing model. Steady-state measurements are initially taken to characterize the flow structure to be used as an initial condition for the gust. All experiments take place in the optical towing-tank facility at Queen's University shown in Figure 2(a). The tank has a 1 m by 1 m cross-section, and is 15 m long. To minimize free-surface effects, the tank has a roof section with a small slit that provides only enough space for a sting to pass. Axial accelerations approximate a ramp function from Re = 300,000 to Re = 450,000 over the range $1 < g^* < 6$, where g^* is the normalized distance over which the gust takes place, normalized by the centre-span chord. Absolute distance travelled is also normalized by centre-span chord, denoted by $s^* = s/c$. An s^* value of zero is refers to the instant the acceleration begins. Figure 3(a) shows the range of gust magnitudes tested, where the models initial velocity is U = 1 m/s. Figure 3(b) shows that the traverse is capable of faithfully replicating a ramp motion up to $g^* = 0.75$ (with 3-5% steady state error).

2.1. FORCE, MOMENT AND PRESSURE

The model has a centre-span chord of 0.3 m, a sweep angle of 45°, and is selective laser sintered (SLS) from nylon plastic material. The wing is treated 110 with cyanoacrylate to seal the porous surface, preventing water ingress into the inner volume. Sixteen 3.175 mm ID passages are printed directly into the model body, each with d = 1.588 mm tap diameter, and 3.175 mm depth. Tap diameter is sized yielding $d^+ = 300$. Pressure taps are spaced 0.2 chords in the streamwise direction, and 0.1 chords in the spanwise direction. The tap locations span $0.2c < x < 0.8c$, and $0.1c < z < 0.7c$, positioned as displayed in Figure 4(a). Pressure tubing is daisy-chained such that differential measurements are taken between taps, with absolute pressure only measured from the first tap near the leading edge. Four Omega PX409 bi-directional differential pressure transducers and one Omega PX419 absolute vacuum traducer 125 permitted measurement of five taps simultaneously. The transducers have a response time of < 0.001 s, and a claimed accuracy of 0.08% of best straight line

(BSL) linearity, hysteresis and repeatability combined. The pressure transducer daisy chain configuration is shown in Figure 4(b), with the fourth differential sensor omitted for clarity. The time-resolved surface pressure is plotted using a cubic interpolation over the spatial domain of the taps. A uniform grid representing a cubic surface, G = f(x, z), is fit to the point data at each pressure tap location. The interpolated surface always passes through the data points measured at each pressure tap. Pressure coefficient, Cp, is calculated using the instantaneous freestream velocity throughout the gust. An ATI Nano 25 six-axis force sensor is mounted at the center-chord, on the symmetry plane of the NACA0012 profile as shown in Figure 4(a). The transducer has a static resolution of 0.125 N, with forces and moments sampled at a rate of 1000 Hz for all runs. Steady state forces are averaged over 5 runs, and 10 chords traveled. For each run, the model is accelerated from rest over 3 chords (g∗ = 3), followed by additional 14 chords at a constant velocity before averaging. The steady measurements indicate a minimum of 10 chords of travel to reach steady state. Therefore, 14 chords of travel would be sufficient to guarantee a steady initial condition for the gust measurements. The additional 4 chords traveled are also used to verify that the steady portion of the gust measurements agreed with the initial steady measurements. Measurements of the gust cases are averaged over 25 runs. A 100-point span Savitzky-Golay filter is applied to the transient force and moment data, in order to smooth noise at high frequencies not relevant to the mean flow behavior.

2.2. PARTICLE IMAGE VELOCIMETRY

Time-resolved planar PIV measurements are conducted at three spanwise planar sections, z/c = 0.1, 0.3, and 0.5. The approximate field of view (FoV) size is 40 cm Å~ 30 cm, or 1.33 chords in length, and 1 chord in height. Angles of attack are selected based on force and moment measurements, which show clear changes between 20◦ and 30◦. Particle images are captured at 1500 Hz using a Photron SA4 camera with 1024Å~1024 pixel resolution. A 40 mJ/pulse Photonics Industries laser is synchronized to the camera frame rate, with a sheet thickness of approximately 1.5 mm. PIV and pressure measurements are taken simultaneously, and ensemble averaged over 20 runs for each FoV. Velocity and vorticity fields are normalized by instantaneous freestream velocity throughout the gust.

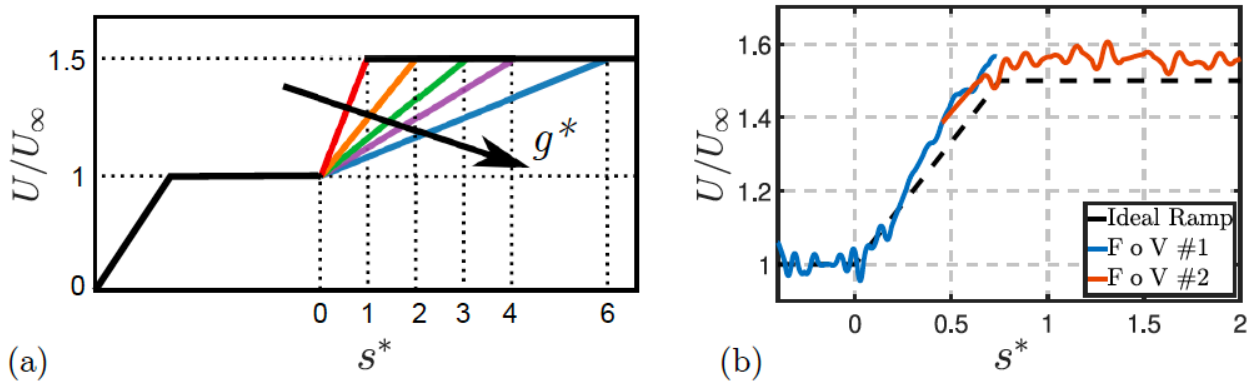

Figure 15-3: (a) A ramp motion represents a gust in which a steady-state model rapidly accelerates in the streamwise direction from Re = 300,000 to Re = 450,000. Gust magnitude is designated by g∗ , model distance travelled in chords is represented by s∗ , and velocity is normalized by the initial freestream velocity. (b) The maximum possible gust magnitude achievable with the model rig in the towing tank at 20º incidence is approximately g∗ = 0.75. 3-5% steady state error is observed at the target velocity.

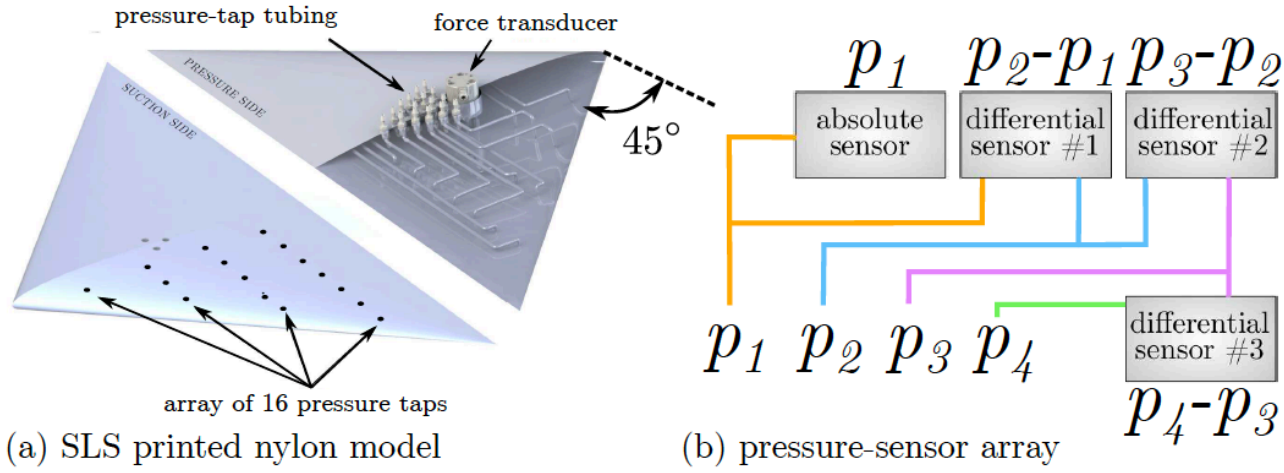

Figure 15-4: (a) Selective laser sintering (SLS) printed nylon delta wing model with 45º sweep. (b) Four differential pressure sensors are daisy-changed, referencing a single absolute sensor, allowing for direct measurement of the pressure gradient across taps (fourth differential sensor omitted for space/clarity).

RESULTS

A sweep of gusts ranging from $g^* = 1$ to $g^* = 6$ are conducted at $\alpha = 20^o$ and $\alpha = 30^o$ angles of attack. Force histories at $\alpha = 20^o$ quickly converge to steady-state following termination of the gust. Figure 5(a) shows that force and moment response varies linearly with gust magnitude. In contrast, at $\alpha = 30^o$, a bifurcation in force response occurs between $g^* = 2$ and $g^* = 1$. Proceeding the latter, is a sustained increase in lift, drag, and pitching moment for six chords of travel. Furthermore, Figure 5(b) shows that the lift and drag forces do not collapse for $g^* = 1$. Most interestingly however, is an inflection that occurs before peak values are reached. The remaining gusts from $2 < g^* < 4$ exhibit less drastic behavior, with peak forces collapsing along the same curve.

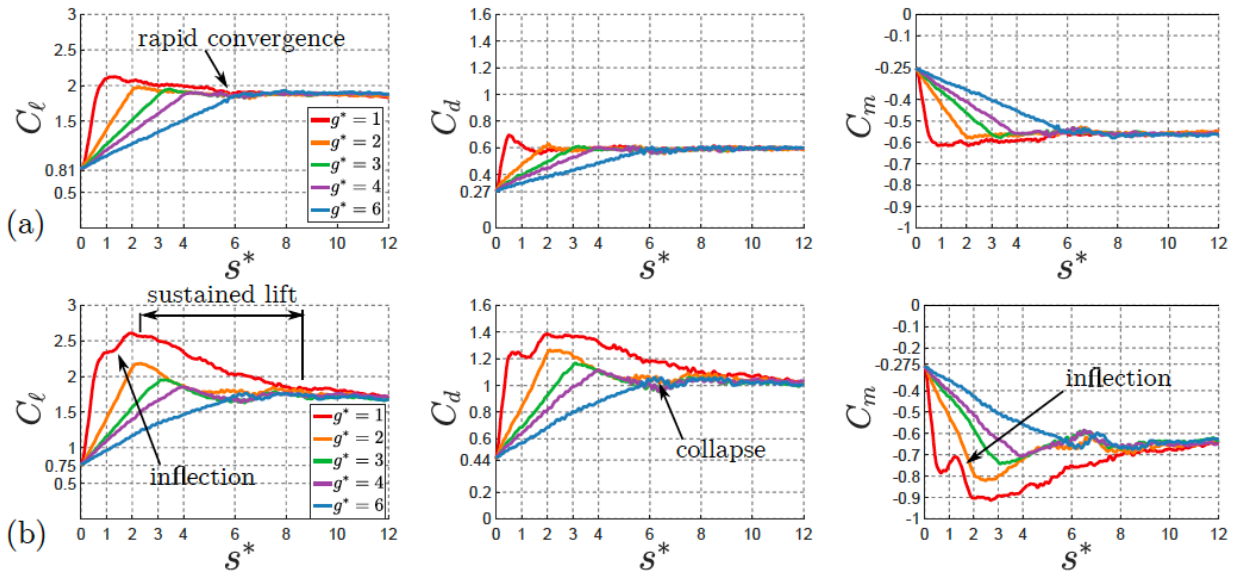

Figure 15-5: Lift, drag, and moment response to a range of gusts (1 < g∗ < 6) at (a) α = 20° and (b) α = 30°.

In consideration of the unsteady force results, evolution of the velocity-field for g∗ = 1 and g∗ = 2 gusts are compared and shown in Figure 6. Prior to the gust, at α = 20°, the flow remains mostly attached, and only at the z/c = 0.5 plane does the shear layer totally separate from the wing surface. During the gust, in the sections where the flow is initially attached, there is an increase in instantaneous velocity, but no flow structure is shed. At α = 30°, the flow is characterized by fully separated shear layers at the gust onset. During the gust, reattachment of these separated shear layers is responsible for the bifurcation in force history. Moreover, this behavior is not consistent across the span of the wing (see Figure 6). At the inboard sections (z/c = 0.1, 0.3), it appears that the effect of the gust is to increase vorticity flux at the leading edge, causing the shear layer to reattach approximately at the quarter-chord position (x/c = 0.4). Vorticity concentration at the leading edge appears to increase during the gust and Figure 7 shows the reattached shear layer halfway through the gust. At z/c = 0.5, the shear layer never reattaches regardless of gust magnitude. Instead, the shear layer rolls up into a vortex, that is in turn shed before the gust ends. The vorticity field in Figure 7 shows the shear layer feeding the leading-edge vortex on the z/c = 0.5 section. Midway through the gust (s∗ = 0.5), the shear layer on both the z/c = 0.1 and 0.3 sections stagnate on the wing surface at approximately x/c = 0.3, resulting in a temporary rise in pressure at this location. The rise in pressure corresponds to the inflection observed in the lift and drag history seen in Figure 5(b). Peculiarly, for α = 30° and g∗ = 1, lift continues to rise after the gust has ended, suggesting that the flow remains attached long after the gust has terminated. Further evidence supporting this sustained attachment is provided by the strong favorable pressure gradient that forms near the leading edge. This favorable pressure gradient drives the flow to remain attached where it is normally separated at steady-state.

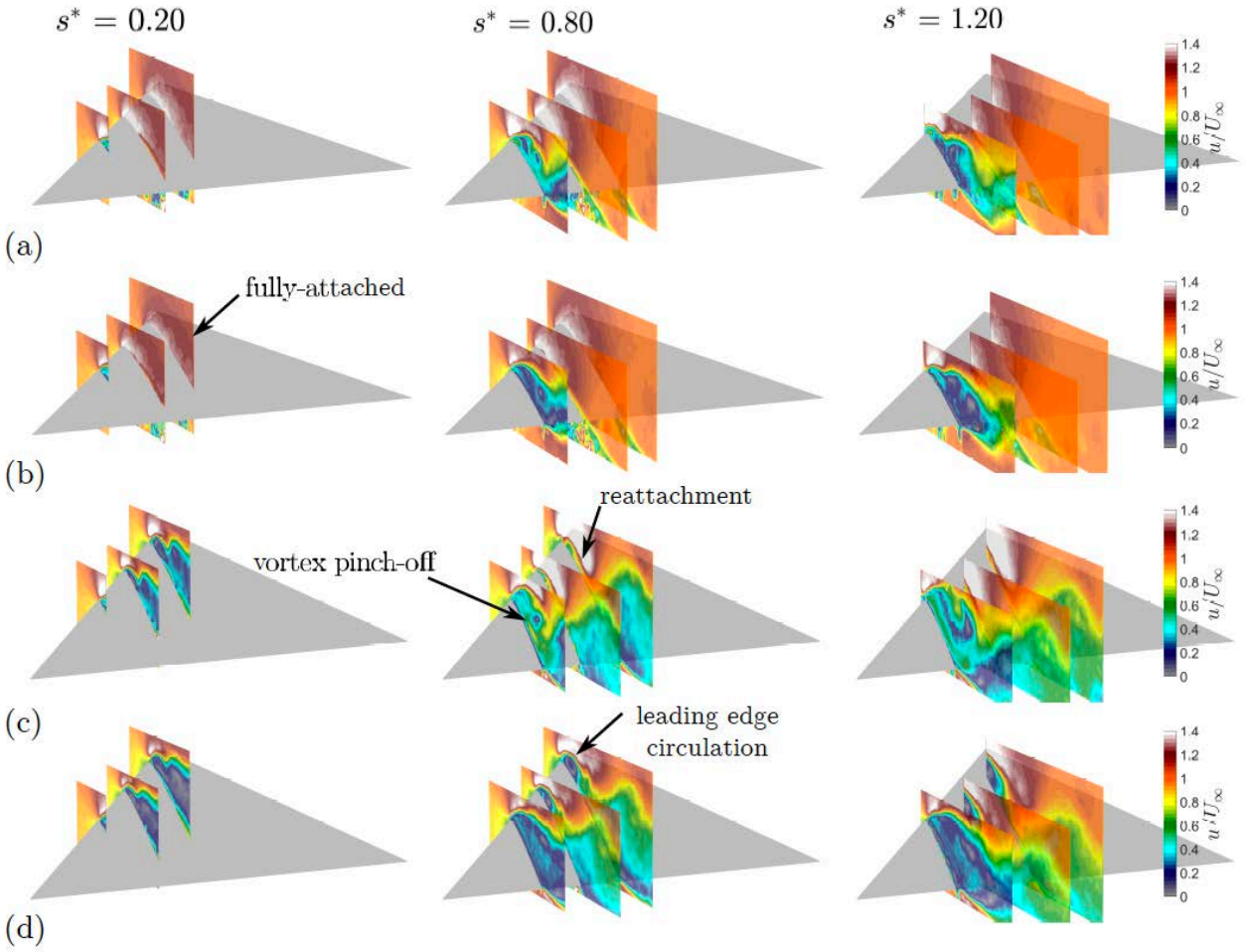

Figure 15-6: Evolution of flow over the gust duration for (a) α = 20◦, g∗ = 1, (b) α = 20◦, g∗ = 2, (c) α = 30◦, g∗ = 1, (d) α = 30◦, g∗ = 2.

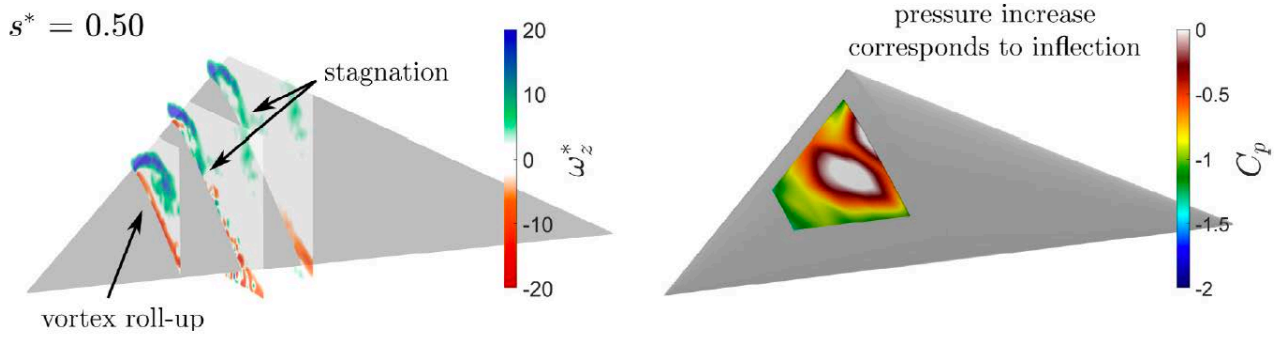

Figure 15-7: Vorticity field and surface pressure at α = 30◦, g∗ = 1 demonstrating mechanism of dynamic flow reattachment and corresponding pressure increase.

CONCLUSIONS

The dynamic stall induced by streamwise gusts on non-slender delta wings is investigated experimentally. A NACA0012 cross-section, 45^{o} sweep model serves as the canonical geometry, and acceleration is used in place of varying inflow conditions. Forces, surface pressure, and planar PIV measurements are conducted simultaneously to capture the flow evolution. Force augmentation both during and after the gust is shown to be dependent on the structure of separated shear layers at the onset of the gust, with strong sensitivity to gust magnitude exhibited at a 30◦ angle of attack. During the gust, separated shear layers near the wing apex reattach, causing enhancement of lift, drag, and moments well beyond the end of the gust period. Drawing parallels to accelerating spheres (Fernando et al. (2017)), the separation line on the delta wing moves downstream until complete reattachment is achieved on the z/c = 0.3 and 0.1 spanwise sections. However, in contrast to the sphere study, augmented forces are maintained after the gust ends. Immediately following the gust motion, a rapid drop in surface pressure near the leading edge further drives attachment, thereby sustaining force and moment values at this post-stall incidence angle. Disparity to the behavior of accelerating spheres is attributed to the vertical nature of delta wing flows. Trends in leading edge circulation are used to assist in explaining this disparity.

REFERENCES

[1] Brown CE, Michael Jr WH. On slender delta wings with leading-edge separation. NACA Tech Mem 1955.

[2] Cummings R, Schuette A. An integrated computational/experimental approach to ucav stability and control estimation: overview of NATO RTO AVT-161. In: 28th AIAA Applied Aerodynamics Conference. 2010.

[3] Cummings R, Schuette A. Integrated computational/experimental approach to unmanned combat air vehicle stability and control estimation. Journal of Aircraft 2012; 49(6):1542–57.

[4] Earnshaw P, Lawford J. Low-speed wind-tunnel experiments on a series of sharp-edged delta wings. HM Stationery Office, 1966.

[5] Fernando J, Marzanek M, Bond C, Rival D. On the separation mechanics of accelerating spheres. Physics of Fluids 2017; 29(3).

[6] Granlund K, Monnier B, Ol M, Williams D. Airfoil longitudinal gust response in separated vs. attached flows. Physics of Fluids 2014; 26(2).

[7] Gursul I. Review of unsteady vortex flows over slender delta wings. Journal of Aircraft 2005; 42(2): 299–319.

[8] Gursul I, Gordnier R, Visbal M. Unsteady aerodynamics of nonslender delta wings. Progress in Aerospace Sciences 2005; 41(7): 515–57.

[9] Gad-el Hak M, Blackwelder R. The discrete vortices from a delta wing. AIAA Journal 1985; 23(6): 961–2.

[10] Gad-el Hak M, Ho C. The pitching delta wing. AIAA Journal 1985; 23(11): 1660–1665.

[11] He X, Le Provost M ,Williams D. Dynamic active flow control of the roll moment on a generic ucas wing. In: 2018 AIAA Aerospace Sciences Meeting. 2018.

[12] Konrath R, Roosenboom E, Schroeder A, Pallek D, Otter D. Static and dynamic saccon piv tests, part ii: aft flow field. In: 28th AIAA Applied Aerodynamics Conference. 2010.

[13] Lamb H. Hydrodynamics. Cambridge university press, 1932.

[14] Le Provost M, He X, Williams D. Real-time roll and pitching moment identification with distributed surface pressure sensors on a ucas wing. In: 2018 AIAA Aerospace Sciences Meeting. 2018.

[15] Lee M, Ho C. Lift force of delta wings. Applied Mechanics Reviews 1990; 43(9):209–21.

[16] Liebeck RH. Design of the blended wing body subsonic transport. Journal of Aircraft 2004; 41(1):10–25.

[17] Lighthill M. Laminar boundary layers. Oxford University Press, USA 1963: 5–88.

[18] Morton B. The generation and decay of vorticity. Geophysical and Astrophysical Fluid Dynamics 1984; 28(3-4): 277–308.

[19] Ol M, Gharib M. Leading-edge vortex structure of nonslender delta wings at low reynolds number. AIAA Journal 2003; 41(1): 16–132.

[20] Panah AE, Akkala JM, Buchholz JH. Vorticity transport and the leading-edge vortex of a plunging airfoil. Experiments in Fluids 2015; 56(160).

[21] Polhamus E. A concept of the vortex lift of sharp-edge delta wings based on a leading-edge-suction analogy. Technical Report; NASA Tech. Mem.; 1966.

[22] Taylor G, Schnorbus T, Gursul I. An investigation of vortex flows over low sweep delta wings. AIAA Journal 2003.

[23] Zhao Gy, Li Yh, Liang H, Han Mh, Hua Wz. Control of vortex on a nonslender delta wing by a nanosecond pulse surface dielectric barrier discharge. Experiments in Fluids 2015; 56(1): 1864.